Research Article | Vol. 28, No. 19 / 14 September 2020 / Optics Express 27903
Optics EXPRESS

Substrate integrated Bragg waveguide: an octave-bandwidth single-mode hybrid transmission line for millimeter-wave applications

BINBIN HONG,[1,2] NAIXING FENG,[1] JING CHEN,[1] GUO PING WANG,[1,3] VIKTOR DOYCHINOV,[2] ROLAND CLARKE,[2] JOHN CUNNINGHAM,[2] IAN ROBERTSON,[2] AND NUTAPONG SOMJIT[2,4]

[1] *Institute of Microscale Optoelectronics, Shenzhen University, Shenzhen 518060, China*
[2] *School of Electronic and Electrical Engineering, University of Leeds, Leeds LS2 9JT, UK*
[3] *gpwang@szu.edu.cn*
[4] *n.somjit@leeds.ac.uk*

Abstract: We demonstrate an air-core single-mode hollow hybrid waveguide that uses Bragg reflector structures in place of the vertical metal walls of the standard rectangular waveguide or via holes of the so-called substrate integrated waveguide. The high-order modes in the waveguide are substantially suppressed by a modal-filtering effect, making the waveguide operate in the fundamental mode over more than one octave. Numerical simulations show that the propagation loss of the proposed waveguide can be lower than that of classic hollow metallic rectangular waveguides at terahertz frequencies, benefiting from a significant reduction in Ohmic loss. To facilitate fabrication and characterization, a proof-of-concept 20 to 45 GHz waveguide is demonstrated, which verifies the properties and advantages of the proposed waveguide. A zero group-velocity dispersion point is observed at near the middle of the operating band, which is ideal for reducing signal distortion. This work offers a step towards a hybrid transmission-line medium that can be used in a variety of functional components for multilayer integration and broadband applications.

1. Introduction

Recently, the millimeter-wave (mmW) and terahertz (THz) frequency bands have attracted much attention owing to their unique applications, such as ultra-broadband spectroscopic sensing [1], high-data-rate wireless communication [2], imaging and non-destructive testing [3], security screening [4] and radio astronomy [5]. However, the development of practical mmW to THz systems has proved to be challenging due to the lack of high-power radiation sources and high-sensitivity detectors, along with the high loss of planar transmission-line structures. Traditional hollow metallic rectangular waveguides are surprisingly difficult to replace as the main electromagnetic waveguiding medium for the integration of subsystems. There is great interest in finding an alternative transmission-line medium that is low-loss, single-mode, broadband, compact, and has good isolation but is much easier to fabricate and suitable for functional components and multichip modules.

Planar transmission lines are widely used in functional components and multichip modules for realizing passive components and interconnects, but they generally suffer from high substrate and radiation losses at 1 THz and above, as well as mode competition with the substrate modes [6]. Reported propagation loss results for microstrip, coplanar waveguide, coplanar stripline, and

#399160 https://doi.org/10.1364/OE.399160
Journal © 2020 Received 2 Jun 2020; revised 27 Jul 2020; accepted 5 Aug 2020; published 8 Sep 2020

Optics EXPRESS

Goubau line at 1 THz are approximately α_{ms} = 43.3 dB/cm, α_{cpw} = 65.1 dB/cm, α_{cs} = 26 dB/cm, and α_{gl} = 30.4 dB/cm, respectively [7–10]. The dielectric substrate of planar transmission lines supports unwanted TM modes which limit the single-mode operating frequency band. An on-chip THz liquid sensor based on a Goubau line has been reported operating up to 0.8 THz, the highest operating frequency limit of which is mainly determined by the mode competition between the guided mode and surrounding modes in the substrates or superstrates [11]. The propagation loss of rectangular dielectric waveguide has been reported to be less than 0.54 dB/cm between 0.44 and 0.5 THz with a minimum of 0.18 dB/cm occurring at 0.481 THz [12]. The loss is mainly limited by the absorption of the host material, but it still suffers from poor isolation [12,13]. Photonic crystal slab waveguide has been shown to have a loss of about 4 dB/cm between 0.54 and 0.63 THz, but likewise, it suffers from poor isolation and limited bandwidth which is undesirable for multilayer integration and broadband applications [14,15]. Likewise, effective-medium-cladded dielectric waveguide [16], which has been realized at 0.26–0.4 THz with single dominant modes in both orthogonal polarizations with an average measured propagation loss around 0.05 dB/cm, also suffers from poor vertical isolation. Recently, a self-supporting hybrid photonic crystal waveguide has been demonstrated to operate over 0.367–0.411 THz in a single-mode fashion with the propagation loss less than 0.05 dB/mm [17]. It comprises hexagonal silicon photonic crystal walls in the lateral direction sandwiched by parallel gold plates in the vertical direction. Compared with the above-mentioned hybrid photonic crystal waveguide, the work presented in this paper utilizes Bragg reflectors as the sidewalls which have continuous translational symmetry in the longitudinal direction, and hence the photonic bandgap and the related operating bandwidth can be much wider as the wave vector is not restricted in the first Brillouin zone. Substrate-integrated waveguide (SIW) has been reported to be broadband and operate to 0.5 THz with loss less than 3.5 dB/cm by selecting different operating modes at different bands, but it is difficult to metalize the vias in SIW - especially when the vias become very small at short wavelengths [18]. Microstructured fibers, including photonic crystal fibers [19–21], antiresonant fibers [22], porous step-index fibers [23], hollow dielectric-lined fibers [24], etc., have all been reported as promising solutions for low-loss quasi-single-mode THz wave-guiding, but they are as yet relatively bulky and hard to integrate with active devices.

In this paper, we show that millimeter and THz waves can be tightly confined in the air core of a hybrid waveguide that is essentially a hollow rectangular waveguide with Bragg reflectors instead of vertical side walls. By avoiding the vertical walls, the waveguide can be fabricated as a photonic crystal structure on a single planar substrate sandwiched between two parallel ground planes, with no metalized via holes. It is, in essence, a flat form of the well-known Bragg fiber [25] that can be realized on a single substrate and so we call it a Substrate Integrated Bragg Waveguide (SIBW). Since it can be realized on a single substrate it is versatile for designing a variety of functional components based on the highly flexible and expandable photonic crystal structure, such as sensors, filters, H-plan horn antennas, lasers and frequency combs, which has already been successfully demonstrated in optical frequencies [26–30]. Compared with conventional all-dielectric planar Bragg waveguide [31], the proposed SIBW is a hybrid waveguide which offers better signal isolation in the vertical direction benefiting three-dimensional circuit stacking and integration. According to our theoretical analysis, the SIBW operates in the fundamental HE_{10} mode while suppressing the high-order competing modes using a modal-filtering effect, which allows the waveguide to operate in single-mode fashion over more than one octave. Compared with planar transmission line modes, the vertically polarized HE_{10} mode of the SIBW can be more easily coupled with the free-space Gaussian mode or the TE_{10} mode of a rectangular waveguide, which are the most widely used interfaces for THz-TDS or THz vector network analyzer (VNA) systems, respectively. Besides, the SIBW uses dielectric rather than metal in the vertical wall resulting in a lower propagation loss than that of the classic hollow metallic rectangular waveguide. A proof-of-concept millimeter-wave SIBW was designed and tested in

Optics EXPRESS

order to verify the transmission properties of the proposed structure. Although it has a relatively low operating frequency, it verifies the physical mechanisms for octave bandwidth single-mode operation and so demonstrates that this is an important candidate for an octave-bandwidth single-mode transmission line for mmW and THz functional components, such as filters, power dividers, and H-plane horn antennas.

2. Principle

The schematic diagram of the proposed SIBW is illustrated in Fig. 1(a). The top and bottom layers are parallel metal ground planes, and the middle layer is a substrate that realizes an air-core line-defect 1D photonic crystal Bragg reflector structure. The Bragg reflector consists of periodically alternating layers of high- and low-refractive-index materials. Air is chosen as the low-refractive-index material for its low refractive index and low loss. The other material that forms the Bragg reflector is desired to be high refractive index and low loss, to create a large photonic bandgap and reduce the material absorption loss. High-resistivity silicon is one of the most commonly used materials which has high refractive index and low absorption loss in the THz frequency range [32], and thus it is chosen as the high-refractive-index component of the photonic crystal in our theoretical analysis. The fundamental mode of the proposed SIBW is vertically polarized HE_{10} mode, and its electric field is evenly distributed along the z-axis. The height of the SIBW, h, does not contribute to the dispersion relations for vertically polarized modes. Therefore, the dispersion relation problem for vertically polarized modes can be simplified into a two-dimensional (2D) problem in the x-y plane assuming the third dimension is infinite and uniform. To avoid higher-order competing modes, h should be not greater than $w/2$.

To maximize the first-order photonic bandgap which supports operating HE_{10} mode, a and b are chosen based on the following quarter-wavelength condition [33]:

$$n_a a = n_b b = \frac{\lambda_c}{4}, \tag{1}$$

where n_a and n_b are the refractive index of the high- and low-refractive-index materials and λ_c is the center wavelength of the first-order bandgap when the longitudinal propagation constant $\beta = 0$. As we can see from Eq. (1), by properly choosing a target operating wavelength (λ_c) and the materials for the high- and low-refractive-index layers, the geometric parameters of the Bragg reflector structure can change accordingly and the operating band can thereby be scaled to any target operating wavelength. The high-resistivity silicon is dispersionless, and the real part of its complex refractive index is 3.4175 ± 0.00005 between 0.5 and 4.5 THz [32]. Thus, in our theoretical design, $n_a = 3.4175$, $n_b = 1$, $a = \frac{n_b}{n_a+n_b}\Lambda = 0.2264\Lambda$, and $b = \frac{n_a}{n_a+n_b}\Lambda = 0.7736\Lambda$. The width of the line defect in the middle of the Bragg reflector waveguide, w, greatly affects the dispersion curves of the defect modes, but it barely affects the dispersion curves of the cladding modes. The value of w should be carefully chosen to push the dispersion curve of the competing second-order odd mode to the edge of the photonic bandgap, so the competing mode becomes lossy which stops it from being excited in the SIBW. This creates the well-known modal-filtering effect [34] and allows the SIBW operates over more than one octave.

Dispersion curves for vertically (z-axis) linearly polarized modes in the line-defect Bragg reflector waveguide overlaid upon the projected bandgap diagram are shown in Fig. 1(b). For the sake of plotting the projected bandgap diagram with a dimensionless property in Fig. 1(b), the longitudinal propagation constant β is scaled with $2\pi/\Lambda$. The value of $\beta\Lambda/2\pi$ is not restricted between -0.5 and 0.5, as the structure has continuous translational symmetry in the longitudinal direction. Similar to photonic crystal fiber, a complete bandgap is not necessary for the proposed waveguide. Because of the translational symmetry, the propagation constant β is conserved, and it is therefore still useful to have bandgap over some finite range of β [35].

Optics EXPRESS

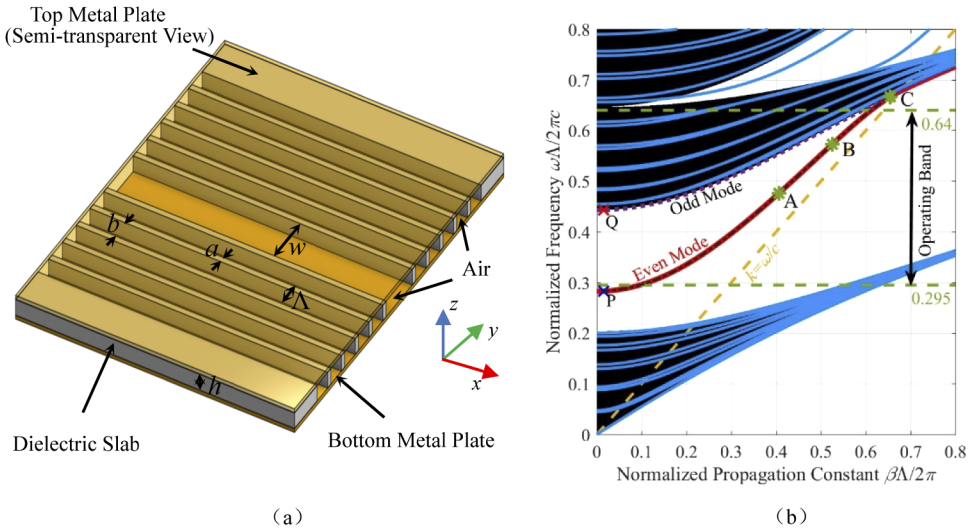

Fig. 1. (a) Schematic diagram of the proposed SIBW with the key design parameters indicated. $\Lambda = a + b$ is the period of the photonic crystal structure. $w = 1.89\Lambda$ is the width of the line defect in the core region. $h \leq w/2$ is the thickness of the dielectric slab. The electric field of the operating mode is mainly z-polarized. (b) Projected bandgap diagram and dispersion curves for the vertically polarized modes in the SIBW. Here, the dielectric slab is silicon, $a = 0.2276\Lambda$, and $b = 0.7724\Lambda$. The orange dashed line is the light line. The green dashed lines indicate the operating band which is wider than one octave. The black region is the bandpass region for the 1D photonic crystal in which the electromagnetic wave can pass through the periodic structure and leak out. The white region above the light line is the bandgap. The red solid line and the purple dotted line represents the dispersion curves for the fundamental HE_{10} mode and the second-order competing HE_{20} mode, respectively. The blue curves overlaid upon the black region are cladding modes or lossy defect modes whose electric field are mainly distributed in the bulk crystal. The black dot-dashed line overlaid upon the red curve represents the 3D full-structure and full-wave simulated dispersion curve of the fundamental mode using COMSOL. Points P, Q, A, B, and C are marked points for later use in Figs. 2 and 4.

The dispersion curves are numerically calculated using the open-source MIT Photonic-Bands (MPB) package [36] and commercial finite element software COMSOL, while the photonic bandgap is calculated separately and analytically according to Bloch's theorem [37]. MPB simulates the above-mentioned 2D simplified structure assuming infinitely extending dielectric lamellae in the z-direction, while COMSOL simulates the 3D full structure taking into account the top and bottom metal plates. From Fig. 1(b), we can see that the dispersion curves of the fundamental guide even mode calculated using both methods are coincident with each other. Thus, the simplified 2D model presents the problem related to vertically polarized modes very well.

The projected photonic bandgap obeys the following condition, which provides the constraint which stops the EM wave from propagating through into the periodic claddings from the line defect [37]:

$$|\mathrm{Re}(X_s)|<1 \tag{2}$$

where

$$X_s = \left[\cos(k_b b) - \frac{i}{2}\left(\frac{\xi_b k_b}{\xi_a k_a} + \frac{\xi_a k_a}{\xi_b k_b}\right)\sin(k_b b)\right]\exp(-ik_a a) \tag{3}$$

Optics EXPRESS

Here, $k_i = \sqrt{(n_i k_0)^2 - \beta^2}(i = a, b)$ is the lateral propagation constant; $k_0 = \omega/c$ is the vacuum wavenumber; β is the longitudinal propagation constant in the x-direction; $n_{eff} = \beta/k_0$ is the effective refractive index of the mode; ω is the vacuum angular frequency; c is the speed of light in vacuum; and ξ_i is 1 or $1/n_i^2(i = a, b)$ corresponding to S = TE or TM modes, respectively.

MPB calculates both the cladding modes, which are mainly distributed in the bulk photonic crystal and the defect modes which are mainly distributed in the central line defect region. As we can see from Fig. 1(b), the dispersion curves for the cladding modes calculated by MPB are coincident with the bandpass region calculated based on Bloch's theorem, validating both methods. The red solid curve corresponds to the desired fundamental HE_{10} mode in SIBW, while the purple dotted line lying at the edge of the photonic bandgap corresponds to the competing and lossy HE_{20} mode. Regarding the $y = 0$ plane, the HE_{10} and HE_{20} modes correspond to the symmetric even mode and antisymmetric odd mode, respectively. The mode pattern of point P for the fundamental HE_{10} mode and point Q for the lossy HE_{20} mode in Fig. 1(b) are shown in Fig. 2. As we can see, only the desired fundamental HE_{10} mode can be tightly confined in the line defect region and propagate along the waveguide, while the HE_{20} mode lying at the edge of the photonic bandgap is very lossy and attenuates in the waveguide. This results in the modal-filtering effect [34], which is similar to the method we used in a THz Bragg fiber to suppress unwanted competing modes [38].

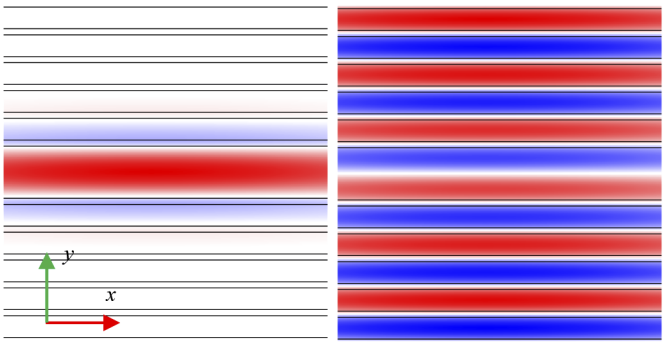

(a) Even mode (b) Odd mode

Fig. 2. Mode patterns (E_z) for points P and Q in Fig. 1(b). (a) Point P: $(\beta_n, \omega_n) = (0.015,\ 0.2828)$; (b) Point Q: $(\beta_n, \omega_n) = (0.015,\ 0.4431)$. Periodic boundaries are applied. Here, $\beta_n = \beta\Lambda/2\pi$ and $\omega_n = \omega\Lambda/2\pi c$.

The frequency range between the two horizontal green dashed lines in Fig. 1(b) gives the operating band of this design. The parts of the dispersion curve for the even mode below the lower dashed line ($\omega_n^l = 0.295$) and above the upper dashed line ($\omega_n^h = 0.64$) are not selected as operating bands since in these frequencies, the guided mode can be relatively lossy and potentially couple to unwanted cladding modes. Here, $\beta_n = \beta\Lambda/2\pi$ and $\omega_n = \omega\Lambda/2\pi c$. The selected operating band gives a ratio bandwidth of $\omega_n^h/\omega_n^l = 2.17$, which is wider than one octave. The group-velocity dispersion (GVD) and the normalized group velocity of the fundamental HE_{10} mode are plotted vs. normalized frequency in Fig. 3. Figure 3 shows that as the frequency increases, the group velocity first increases and then decreases, and the turning point happens to be at $\omega_n = 0.5442$ where the GVD is zero.

Optics EXPRESS

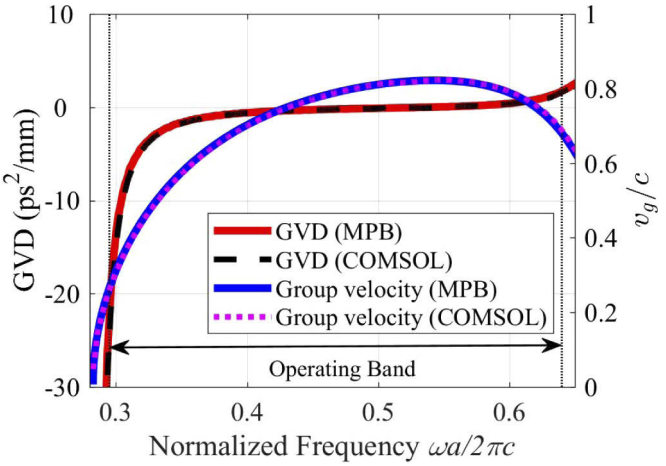

Fig. 3. Group-velocity dispersion ($\partial^2\beta/\partial^2\omega$) and normalized group velocity ($v_g = \partial\omega/\partial\beta$) of the fundamental mode calculated using MPB and COMSOL.

3. Simulation

By choosing $\Lambda = 93.1\mu$m, the operating band of the above-mentioned SIBW is settled around the frequency range of $(\omega_n^l c/\Lambda, \omega_n^h c/\Lambda) = (0.95$ THz, 2.06 THz). In the following simulations, a representative surface roughness equal to 1.5 times of the skin depth of copper is considered. Here, the skin depth of copper is calculated at the central frequency point under the condition of room temperature (293 K) and DC conductivity of 5.967×10^7 S/m. The built-in tabulated impedance model of CST is used to obtain the declined dispersive surface conductivity of copper which is lately used in COMSOL as well to ensure the two numerical packages using same properties of copper. The eigenvalue problem of SIBW is solved using COMSOL. The cross-section of the SIBW is used in COMSOL to find the eigenvalues and eigenmodes, as shown in Fig. 4(a). The dispersion curve of the fundamental HE_{10} mode simulated using COMSOL is plotted in Fig. 1(b) using blue circles, and the GVD and group velocity can be accordingly calculated based on the simulated dispersion relation, as presented using dot-dashed lines in Fig. 3. It can be seen that the COMSOL simulated results agree very well with the MPB calculation which is based on the plane wave expansion method.

The propagation loss of the SIBW is calculated using the following equation [39]:

$$\alpha(\text{dB/cm}) = \frac{1}{5\ln(10)}\frac{\omega}{c}\text{Im}(n_{eff}) \tag{4}$$

where n_{eff} is the effective mode index of the operating fundamental mode obtained from the COMSOL simulation. Figure 4(f) presents the simulated propagation loss of the proposed SIBW, as well as the propagation loss of a standard-size WM-164 hollow copper rectangular waveguide for comparison [40]. The propagation loss of the proposed SIBW is below 3 dB/cm over the frequency range wider than one octave from 0.988 to 2.041 THz, which is much lower than the losses of planar transmission lines [7–10], and even lower than that of the standard-size WM-164 hollow copper rectangular waveguide over a broad band wider than the frequency range from 1 to 2 THz. The propagation loss of SIBW consists of Ohmic loss from metal parts, absorption loss from dielectrics, and radiative loss, which are illustrated as the blue, red, and black zones below the total propagation loss line in Fig. 4(f), respectively. Here, the different loss types are calculated numerically using COMSOL. We first obtained the value of the radiative loss by setting the metal plates as perfect electric conductor (PEC) and the dielectric layers as loss-free

Optics EXPRESS

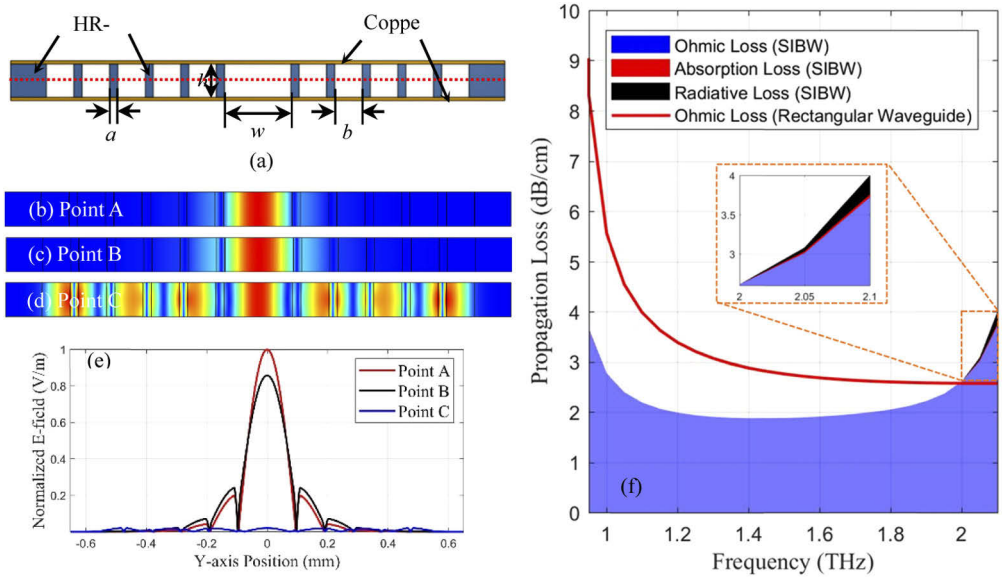

Fig. 4. Structure and characterization of the proposed SIBW. (a) Structure of the SIBW. (b)-(d) Normalized electric field distribution of the desired HE_{10} mode at points A, B, and C shown in Fig. 1(b) and Fig. 4(f). The field linearly decreases from red to blue. (e) Normalized electric field along the red dotted line shown in Fig. 4(a) at selected frequency points. (f) Propagation losses of SIBW and hollow metallic rectangular waveguide. The frequencies of points A, B and C are 1.532 THz, 1.843 THz and 2.154 THz, respectively. The blue, red and black zones represent the proportion of Ohmic loss, absorption loss and Radiation loss in the overall propagation loss. The values of absorption loss and radiative loss are much smaller than the Ohmic loss and are insignificant between 1 THz and 2 THz, so they are barely visible. In the simulation (COMSOL), $a = 0.2264\Lambda \approx 21.7$ μm, $b = 0.7736\Lambda \approx 72$ μm, $w = 1.89\Lambda \approx 176$ μm, and $h = w/2 \approx 88$ μm. The width and height of the hollow metallic rectangular waveguide are 164 μm and 82 μm, respectively.

material. Then, we added the conductivity to the metal parts and the absorption coefficient to the dielectric material separately to identify and calculate the Ohmic loss and dielectric absorption loss, respectively. To clarity, the radiative loss means the loss that leaks into the surrounding space from the Bragg reflectors. It can be seen that the Ohmic loss in the top and bottom copper layers still plays the most significant role. The radiative loss is almost negligible within the operating band, but it increases gradually towards the edges of the operating band, and eventually, the photonic crystal structure loses the ability to confine the electromagnetic wave outside the operating band. The dielectric absorption loss is mainly determined by the absorption coefficient of the dielectric material that constitutes the photonic crystal structure, which is low in this design since the absorption coefficient of high-resistivity silicon is very low over the target frequency range. The dielectric absorption loss is also influenced by the confinement ability of the photonic structure. It can be seen from Fig. 4(f) that, at the high-frequency end of the operating band, the dielectric absorption loss increases with the increase of the radiative loss. This is because when the radiative loss is high, the electromagnetic field penetrates the photonic crystal structure more deeply, and thereby attenuates more significantly by interacting with more dielectric materials. Figures 4(b)–4(d) present the field distributions of the desired HE_{10} mode at several representative frequencies, namely the points A, B and C showed in Fig. 4(f). For the points A and B, the field is mainly confined in the air core and the first period of the photonic crystals structure, while for the point C, which is located at the edge of the operating band, the

Optics EXPRESS

electromagnetic field penetrates further into the photonic crystal structure. Figure 4(e) presents the normalized electric field along the red dotted line shown in Fig. 4(a) at the representative frequencies, which quantitatively confirms the above results.

The effects of number of cladding layers on the propagation losses at selected frequencies are presented in Fig. 5. The three selected frequency points are 1.532 THz, 2 THz, and 1.843 THz, representing the lowest loss point in the middle of the operating band, the edge of the interested operating band, and one point in between. The propagation losses decline with the increase of cladding layer numbers, but they tend to become steady when the number reaches five. In the design, the number of layers is chosen as five to ensure an acceptable and steady confinement, and meanwhile keep the form factor the waveguide as small as possible. The outmost layer is used for supporting the waveguide, as it is treated as a perfectly matched layer in the simulation which can be realized using a relatively thick outmost layer.

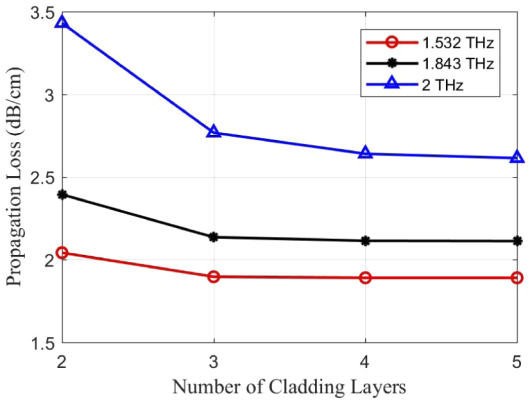

Fig. 5. The dependence of propagation loss on number of cladding layers at selected frequencies.

Wave propagation in the SIBW was studied using commercial package CST Microwave Studio time-domain solver. A hollow metallic rectangular waveguide, whose width (176 μm) and height (88 μm) are equal to those of the defect core of the SIBW, was chosen to feed the SIBW. The single-mode operating frequency range of the hollow metallic rectangular waveguide is between

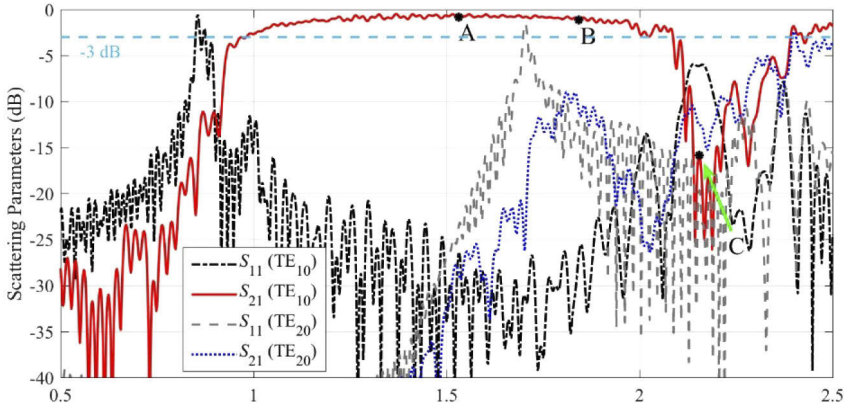

Fig. 6. Scattering Parameters for SIBW when different modes are excited in the hollow metallic rectangular waveguide. The length of the SIBW is 3 mm. Points A, B, and C are the same as those described in Figs. 2 and 4.

Optics EXPRESS

0.85 THz and 1.70 THz, so at frequencies above 1.70 THz, high order modes, such as TE_{20}, TE_{01}, etc., can be excited by the hollow metallic rectangular waveguide.

The scattering parameters for the SIBW when different modes in the hollow metallic rectangular waveguide are excited are shown in Fig. 6. Here, scattering parameters are defined based on voltage ratios of the incident and reflected voltage waves and are in decibel form. From the S_{21} frequency response, when TE_{10} mode is excited we observe that a transmission window wider than an octave centered at about 1.5 THz is supported in the SIBW. The S_{11} response when the TE_{10} mode is excited indicates that the impedance mismatch between the TE_{10} mode in the hollow metallic rectangular waveguide and the HE_{10} mode in the SIBW is low, since the reflection coefficient is basically below −15 dB from 1 to 2 THz. When the second-order TE_{20} mode is excited in the hollow metallic rectangular waveguide at around 1.7 THz, the S_{21} rises but it is still below −9 dB owing to the aforementioned modal-filtering effect, and therefore the high-order mode is suppressed. Under the high-order mode (TE_{20}) excitation condition, the S_{11} is high at around 1.7 THz which means the impedance mismatch is large at the waveguide transition, and at around 2 THz, both S_{11} and S_{21} are relatively small indicating that the second-order mode is leaky in the SIBW because the electromagnetic field is neither reflected nor transmitted. In addition

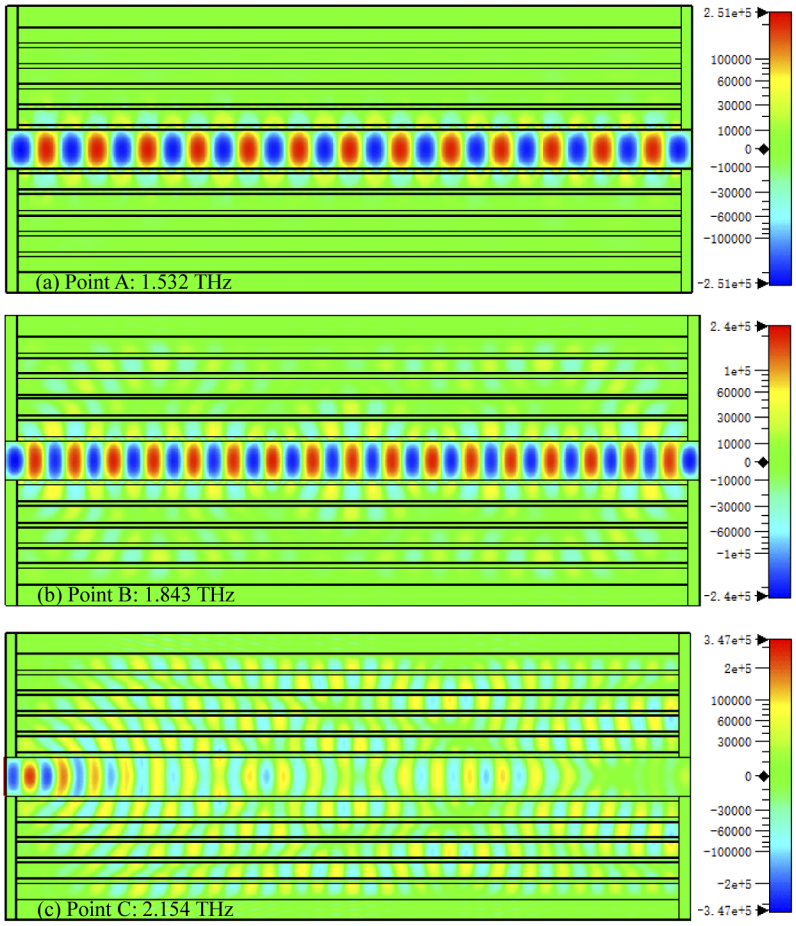

Fig. 7. The z-component of the electric field (E_z) of SIBW at different representative frequencies which corresponds to the points A, B, and C in Fig. 4, respectively. The color bar is in logarithmic scale (unit: V/m).

Optics EXPRESS

to the TE_{20} mode, other high-order modes operate at higher frequencies, which is beyond the frequency range of interest from 1 to 2 THz.

The mode patterns of the guided mode in SIBW at several representative frequencies, namely the points A, B, and C shown in Fig. 4, are shown in Fig. 7. It can be seen that the electric field for both frequency point A and point B can be tightly confined in the central defect region, and the operating mode HE_{10} mode is well preserved along the waveguide for both cases. However, for the frequency point C, the electric field penetrates the cladding layers strongly and the guided mode is no longer the single HE_{10} mode. Comparing (a) with (b) in Fig. 7, the electric field at the point B is slightly leakier than that at the point A, and thus the propagation loss at the point B is larger than that at the point A, as shown in Fig. 4. It is common for photonic crystals that the confinement loss is usually smaller at the middle of a photonic bandgap than that at the edge [38].

The distribution of the surface current density in the SIBW at point A is shown in Fig. 8(a). The surface current density is mainly distributed along the central defect region and the first cladding layer, with the remaining small portion being distributed in the outer cladding layers. There is no free current flow between the top and bottom metal plates, in contrast with both the hollow metallic rectangular waveguide and substrate integrated waveguide. Instead, there is displacement current in the dielectric structure that closes the current loop, so generating the magnetic field as shown in Fig. 8(b).

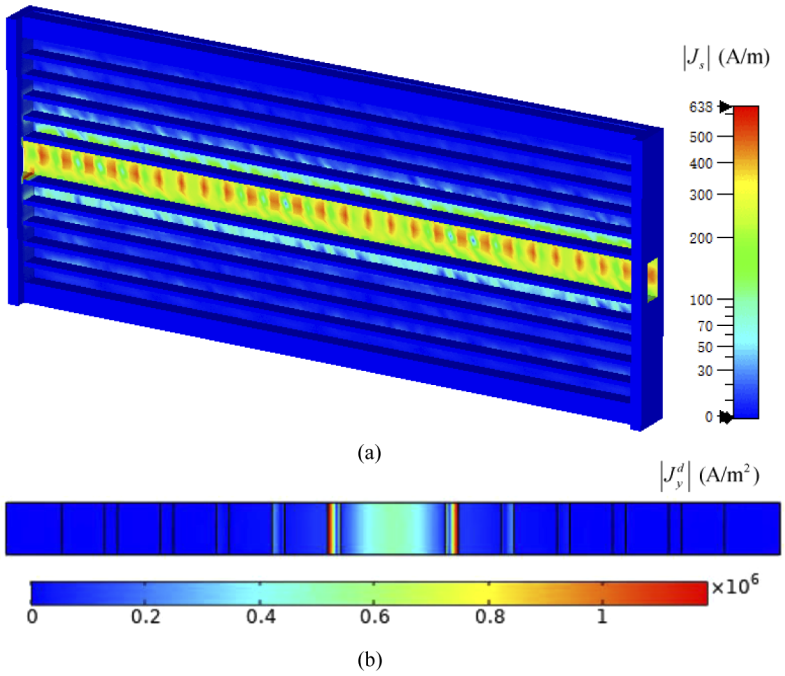

Fig. 8. The current distribution of the SIBW. (a) The magnitude of the surface current at 1.532 THz calculated using CST. (b) The magnitude of the y-component of the displacement current density in the cross-section plane of the SIBW calculated using COMSOL.

4. Scaled experimental verification

To facilitate the fabrication and measurement, a proof-of-concept experimental demonstration of SIBW was performed at millimeter-wave frequencies (ranging from 20 to 45 GHz). Two SIBW samples with different lengths and fed by microstrip and coaxial launchers were fabricated and tested, as shown in Fig. 9. The design principles are the same as those discussed in the principle

Optics EXPRESS

section. The dielectric material used for the SIBW is Rogers RO3010, which has a dielectric constant of 10.2 and loss tangent of 0.0022 over the frequency range from 8 to 40 GHz. The reason why we use the Rogers RO3010 substrate rather than high-resistivity silicon is that the PCB board is compatible with standard PCB fabrication techniques. The similarities between the RO3010 and the high-resistivity silicon are that they both have relatively high dielectric constant and low absorption loss, which are desirable for constructing the designed photonic crystal structure.

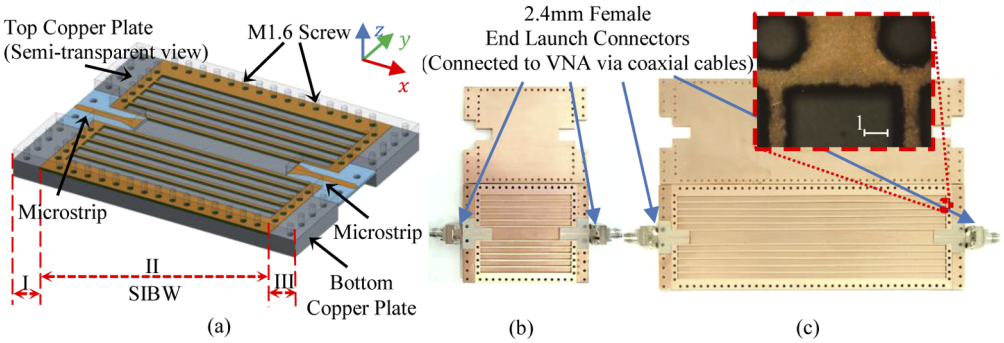

Fig. 9. CAD design and fabricated samples (before assembling) of the SIBW. (a) CAD design. The SIBW in region II is fed by microstrips in regions I and III. (b) Short SIBW with the length between the two microstrip lines l = 46.54 mm. (c) Long SIBW with l = 150.56 mm. The inserted picture in (c) shows the zoomed view of the photonic crystal structure. In the design, a = 1 mm, b = 3.28 mm, w = 8.14 mm, and h = 0.671 mm

In the two samples shown in Fig. 9, both the microstrip feed lines and the photonic crystal structures were machined using laser direct writing technology with the LPKF ProtoLaser U3. The edges of the laser cutting trajectory were slightly burnt and the burnt dielectric material was left on the structure. The substrates for the microstrip and photonic crystal structure are double-sided copper-clad Rogers RT/Duroid 5880LZ (ε_r = 2) and RO3010 (ε_r = 10.2), respectively. The thicknesses of the dielectric and copper claddings of both substrates were 0.635 mm and 17.5 µm, respectively. The copper claddings of the RO3010, which are far thinner than the operating wavelength, were not removed from the dielectric in order to provide extra mechanical support for the delicate photonic crystal structure, and should have negligible impact on the dispersion relation of the SIBW, and only very slightly increase the overall propagation loss, as confirmed by our simulations. The top and bottom copper plates are made of C101 copper. The copper plates were first machined with a DMU 40 CNC milling machine and then manually polished by using 500-Grit wet-and-dry silicon carbide sandpaper. The bottom plates still had visible residual CNC milling tool marks on the surface, the surface finish of the top plates was smooth.

A two-tier calibration technique was used to characterize the SIBW. The first-tier SOLT calibration was performed using a 2.4 mm mechanical calibration kit to place the reference planes to the input interface of the end launch connectors. A second-tier calibration used multiline calibration [41] to de-embed using the complex propagation constant of the SIBW. The two SIBW samples were tested using a vector network analyzer and the scattering parameters are shown in Fig. 10(a). The ripples on the S-parameter responses are mainly due to the impedance mismatches at the interfaces of waveguide transitions and inevitable fabrication imperfections. From the S_{11} for the short SIBW in Fig. 10(a), we can clearly observe two ripple patterns with difference periods in the frequency spectrum. The short period ripple has a period of approximately 1.3 GHz and the long period ripple has a period of about 5.2 GHz. The short period ripple corresponds to the Fabry-Perot resonance between the two interfaces between the SIBW and the microstrip,

Optics EXPRESS

while the long period ripple corresponds to the Fabry-Perot resonance between the input and output interfaces of the microstrips. The S_{11} for the long SIBW also has similar superposed ripple pattens. The long period ripple of the long SIBW has almost same period as that of the short SIBW, which reflects that both SIBWs use same feeding microstrip design. The short period ripple of the long SIBW has shorter period and weaker oscillation than those of the short SIBW as the signal travels longer and attenuates more in the long SIBW. These also explain the origins of the ripples in the raw measurement result for the propagation loss in Fig. 10(d), which also shows superposed ripple patterns with similar periods as that of the S_{11} for the short SIBW. It should be noted that the propagation loss is related to both SIBWs and should reflects the ripples for both cases, but due to the short period ripple of the long SIBW is relatively weak, it is much less observable in the propagation loss curve. The reflection coefficients (S_{11}) of the two SIBWs are lower than −6 dB (<25%) over the frequency of interest between 20 and 45 GHz, which means that a significant amount of the power was fed into the SIBWs. Besides, the magnitude of the S_{11} parameters for the short and long SIBWs are at the same level, which means that the repeatability of the microstrip to SIBW transitions for both SIBWs are acceptable for multiline calibration. The transmission coefficients (S_{21}) for both SIBWs show wideband transmission windows ranging from 20 to 45 GHz which are wider than one octave.

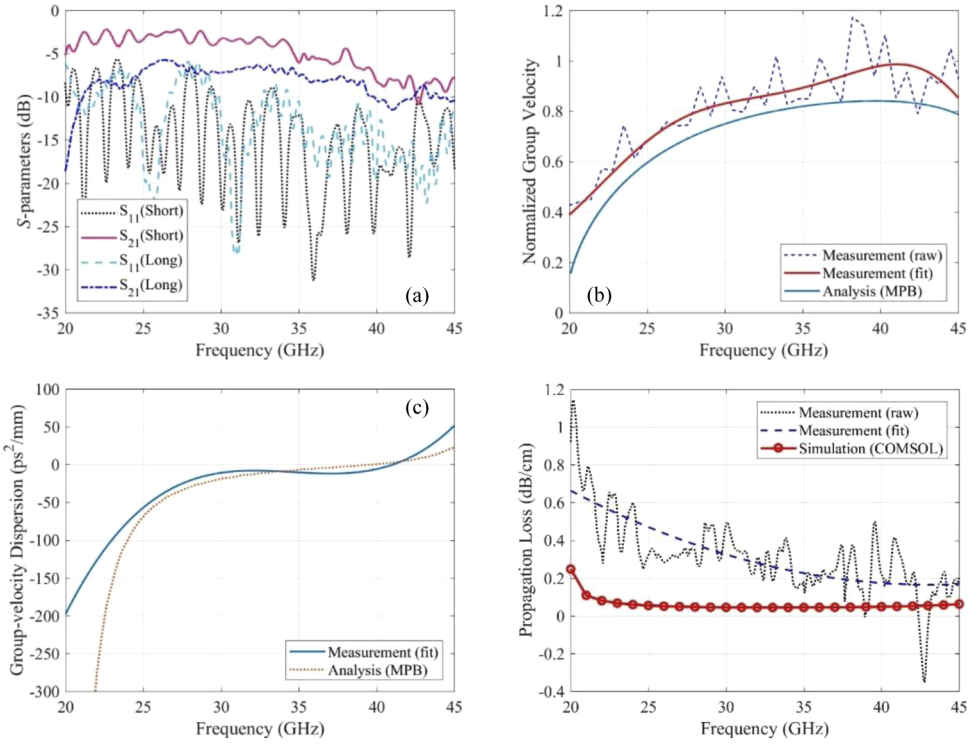

Fig. 10. Characterization of the SIBW. (a) Measured S-parameters of the two SIBW samples. One percentage moving window smoothing, a built-in feature of the VNA, is applied to reduce the very high-frequency ripples due to minor impedance mismatches at fabrication imperfections. (b) Normalized group velocity (v_g/c). Fourth-order polynomial curve fitting is applied to fit the measured normalized group velocity. (c) Group-velocity dispersion ($\partial^2\beta/\partial w^2$). The measurement result is extracted based on the fitted curve for the normalized group velocity shown in Fig. 10(b). (d) Simulated and measured propagation loss. Second-order polynomial curve fitting is applied to fit the measured propagation loss.

Optics EXPRESS

The complex propagation constant of the SIBW can be extracted from the S-parameters shown in Fig. 10(a) using the multiline calibration technique [41,42]:

$$\gamma = \frac{\ln(\chi)}{\Delta l}, \tag{5}$$

where $\gamma = \alpha + i\beta$ is the complex propagation constant, α is the attenuation constant in np/m units, β is the phase constant in rad/m units, Δl is the length difference of the two SIBWs, and χ is the first eigenvalue of the matrix $T^l(T^s)^{-1}$. Here, T^s and T^l are the T-parameters of the short and long SIBWs including the waveguide transition parts, respectively, which can be obtained from the measured S-parameters of the two SIBWs.

The theoretically analyzed and experimentally measured normalized group velocity ($v_g/c = \partial\omega/\partial\beta/c$) of the SIBW can be extracted from the dispersion curve calculated using MPB and the measured phase constant based on the Eq. (5), as shown in Fig. 10(b). Since small ripples on the spectrum of phase constant owing to the small impedance mismatches at discontinuities of the SIBWs or the calibration errors due to the inconsistencies of the two SIBWs have significant impacts on its first-order derivative (v_g), reduced frequency points are used when calculating the group velocity so as to analyze the overall trend of the group velocity. The ripples on the curve of the normalized group velocity, which also makes the normalized group velocity larger than one at several frequencies, attributes to the residual and inevitable small impedance mismatches and calibration errors. The 4th-order polynomial fitted measured curve shows the average trends of the normalized group velocity, which agrees with the theoretically analyzed results according to the dispersion relations of SIBW calculated by using MPB. The reason of using 4th-order polynomial curve fitting to the normalized group velocity is due to the factor that the group-velocity should be one order higher than the GVD which follows the trends of a 3rd-order polynomial fitted curve (as shown in Fig. 3). Both the theoretically analyzed and the experimentally measured normalized group velocity rise firstly with increasing frequency and decrease after reaching a maximum. The maximum points for the theoretical and experimental results are 39.73 GHz and 41.05 GHz, respectively, which are close to each other. The turning points in the normalized group velocity respond correspond to the zero GVD point.

To demonstrate the SIBW operates in the desired fundamental HE_{10} mode over the frequency range from 20 GHz to 45 GHz, we measured the GVD and compared it with the theoretical predictions. Figure 10(c) shows the GVD of the SIBW. The measurement results are calculated using $\partial^2\beta/\partial^2\omega$ based on the fitted measurement results of group velocity in Fig. 10(b). The theoretically analyzed results are obtained according to the dispersion relations of SIBW calculated by using MPB, which has also been adopted in Fig. 3. It can be seen from Fig. 10(c) that the theoretically analyzed and experimentally measured GVDs are at the same level and follow similar trends. A zero GVD point is observed for both theoretical and experimental results, occurring at 39.73 GHz and 41.05 GHz, respectively.

The simulated and measured propagation losses of the SIBW are shown in Fig. 10(d). The measured propagation loss is calculated using $20\log_{10}(e) \cdot \alpha$ according to the Eq. (5). The simulated results are obtained based on a COMSOL simulation similar to that used in Fig. 4(f). In general, the measured and fitted simulated results follow similar trends, namely, the propagation losses decrease firstly with increasing frequency and then increases after reaching a minimum. On average, the measured propagation loss of the fabricated SIBW is less than 0.66 dB/cm (compared with 0.25 dB/cm simulated) over the frequency range from 20 to 45 GHz, which is wider than one octave. The measured loss is observed to be greater than the simulated results, which may due to several factors that increase the loss such as surface roughness, oxidation of the copper layer, residual burnt dielectric material, and fabrication or assembly imperfections. At around 42.8 GHz the propagation loss is below zero due to a dip in the response which is a measurement artifact. Comparing with Fig. 10(a), we can see that at the same frequency point, the S_{21} of the short SIBW declines and the S_{11} of the short SIBW rises abnormally, while for the

Optics EXPRESS

long SIBW, it does not behave in the same way at this frequency. This implies that there is a physical inconsistency between the two SIBWs resulting in multiline calibration errors at around 42.8 GHz, which could be avoided by improving the fabrication and assembly precision.

In summary, we performed a proof-of-concept experimental verification of the guidance mechanism of the proposed SIBW at millimeter-wave frequencies. Table 1 shows the properties of various representative millimeter-wave and terahertz flat waveguides. Compared with other flat waveguides, the proposed SIBW is able to transmit broadband signal with good isolation and relatively low loss. The proposed SIBW require not metal vias and can be realized in a single substrate, which is favorable for fabrication. We found that the measurement results agree with theoretical analysis, which means that the SIBW can operate in single-HE10-mode fashion over a bandwidth wider than one-octave, with a GVD passing through zero close to the middle of the operating band. Benefitting from the vertically polarized operation mode, SIBW can easily couple with free-space sources using lenses or antennas, or on-chip/in-waveguide sources with the help of tapered impedance matching structures. Though the measured propagation loss is slightly higher than the simulated one, as presented in Fig. 10(d), they both follow similar trends. The propagation loss can be further improved and a THz design implemented by using more precise fabrication and assembly techniques, such as deep reactive ion etching (DRIE) and wafer-bonding techniques. THz time-domain spectroscopy is a useful tool for wideband characterization of such a waveguide, which will be further discussed in our future work.

Table 1. Comparison of flat waveguides at millimeter-wave and terahertz frequencies

	Frequency (GHz)	Bandwidth ratio[a]	Propagation loss (dB/cm)	Zero GVD point	Isolation
Microstrip [7]	DC ~ 1000	-	< 43.3	Nearly	Medium
Coplanar waveguide [8]	DC ~ 1000	-	< 65.1	Nearly	Medium
Coplanar stripline [9]	DC ~ 1200	-	< 26	Nearly	Medium
Goubau line [10]	750 ~ 1100	-	< 30.4	Nearly	Poor
Dielectric strip [12]	440 ~ 500	12.77%	~ 0.087	No	Poor
Photonic crystal slab waveguide [15]	540 ~ 630-	15.38%	~ 4	Yes	Medium
Effective dielectric strip [16]	260 ~ 400	32.56%	< 0.05	No	Poor
Hybrid photonic crystal waveguide [17]	367 ~ 411	11.31%	< 0.5	Yes	Good
CPW & SIW [18]	150 ~ 500	107.69%	3 ~ 3.5	No	Good
This work[b]	1000 ~ 2000 (20~45)	66.67% (76.92%)	< 2.78 (< 0.66)	Yes	Good

[a]Bandwidth ratio refers to the absolute bandwidth divided by the central frequency.
[b]The values in the parentheses corresponds to the proof-of-concept measurement results.

5. Conclusions

This paper presents a substrate integrated Bragg waveguide that can operate in single-HE_{10}-mode over more than one octave and in zero group-velocity dispersion fashion around the middle of the operating band. First, we theoretically investigated the SIBW between 1 to 2 THz, and the propagation loss of the proposed SIBW is found to be even lower than that of a classic hollow metallic rectangular waveguide, benefiting from the reduction of Ohmic loss. To facilitate the fabrication and measurement, we performed a proof-of-concept experimental demonstration at millimeter-wave frequencies ranging from 20 to 45 GHz to verify the guidance properties of the proposed SIBW, such as the operating bandwidth, GVD, operating mode, and propagation loss, with consistency between the theoretical analyses (both MPB and COMSOL) and the

Optics EXPRESS

experimental measurements being observed. Showing many advantages over conventional THz planar waveguides, the proposed SIBW is a promising hollow hybrid transmission line for broadband submillimeter-wave and THz systems using functional components or multilayer multichip module technology.

Funding

National Natural Science Foundation of China (11734012, 51601119); Science and Technology Planning Project of Guangdong Province (2020B010190001); Young Innovative Talents Projects of Universities in Guangdong Province (2019KQNCX123); Natural Science Foundation of Shenzhen University (2019006, 860-000002110422); Engineering and Physical Sciences Research Council (EP/P021859/1, EP/R00501X/1).

Acknowledgments

The author would like to acknowledge Dominic Platt and Lei Shi for their helpful discussion, and also thank Graham Brown and Andrew Pickering from the Engineering and Physical Sciences Research Council (EPSRC) National Facility for Innovative Robotic System for their timely help in fabrication.

Disclosures

The authors declare no conflicts of interest.

References

1. P. U. Jepsen, D. G. Cooke, and M. Koch, "Terahertz spectroscopy and imaging–Modern techniques and applications," Laser Photonics Rev. **5**(1), 124–166 (2011).
2. H. J. Song and T. Nagatsuma, "Present and future of terahertz communications," IEEE Trans. Terahertz Sci. Technol. **1**(1), 256–263 (2011).
3. D. M. Mittleman, "Twenty years of terahertz imaging," Opt. Express **26**(8), 9417–9431 (2018).
4. S. S. Dhillon, M. S. Vitiello, E. H. Linfield, A. G. Davis, M. C. Hoffmann, and J. Booske, "The 2017 terahertz science and technology roadmap," J. Phys. D: Appl. Phys. **50**(4), 043001 (2017).
5. C. Kulesa, "Terahertz spectroscopy for astronomy: From comets to cosmology," IEEE Trans. Terahertz Sci. Technol. **1**(1), 232–240 (2011).
6. I. Robertson, N. Somjit, and M. Chongcheawchamnan, *Microwave and millimetre-wave design for wireless communications*, (John Wiley & Sons, 2016).
7. H. M. Heiliger, M. Nagel, H. G. Roskos, H. Kurz, F. Schnieder, W. Heinrich, R. Hey, and K. Ploog, "Low-dispersion thin-film microstrip lines with cyclotene (benzocyclobutene) as dielectric medium," Appl. Phys. Lett. **70**(17), 2233–2235 (1997).
8. M. Y. Frankel, S. Gupta, J. A. Valdmanis, and G. A. Mourou, "Terahertz attenuation and dispersion characteristics of coplanar transmission lines," IEEE Trans. Terahertz Sci. Technol. **39**(6), 910–916 (1991).
9. D. R. Grischkowsky, "Optoelectronic characterization of transmission lines and waveguides by terahertz time-domain spectroscopy," IEEE J. Sel. Top. Quantum Electron. **6**(6), 1122–1135 (2000).
10. J. Cabello-Sánchez, H. Rodilla, V. Drakinskiy, and J. Stake, "Transmission Loss in Coplanar Waveguide and Planar Goubau Line between 0.75 THz and 1.1 THz," In *2018 43rd International Conference on Infrared, Millimeter, and Terahertz Waves (IRMMW-THz)* (pp. 1–2). IEEE (2018).
11. M. Swithenbank, A. D. Burnett, C. Russell, L. H. Li, A. G. Davies, E. H. Linfield, J. E. Cunningham, and C. D. Wood, "On-Chip Terahertz-Frequency Measurements of Liquids," Anal. Chem. **89**(15), 7981–7987 (2017).
12. A. Malekabadi, S. A. Charlebois, D. Deslandes, and F. Boone, "High-resistivity silicon dielectric ribbon waveguide for single-mode low-loss propagation at F/G-bands," IEEE Trans. Terahertz Sci. Technol. **4**(4), 447–453 (2014).
13. N. Ranjkesh, M. Basha, A. Taeb, and S. Safavi-Naeini, "Silicon-on-glass dielectric waveguide—Part II: For THz applications," IEEE Trans. Terahertz Sci. Technol. **5**(2), 280–287 (2015).
14. K. Tsuruda, M. Fujita, and T. Nagatsuma, "Extremely low-loss teraertz waveguide based on silicon photonic-crystal slab," Opt. Express **23**(25), 31977–31990 (2015).
15. H. Amarloo and S. Safavi-Naeini, "Terahertz Line Defect Waveguide Based on Silicon-on-Glass Technology," IEEE Trans. Terahertz Sci. Technol. **7**(4), 433–439 (2017).
16. W. Gao, X. Yu, M. Fujita, T. Nagatsuma, C. Fumeaux, and W. Withayachumnankul, "Effective-medium-cladded dielectric waveguides for terahertz waves," Opt. Express **27**(26), 38721–38734 (2019).

Optics EXPRESS

17. H. Li, M. X. Low, R. T. Ako, M. Bhaskaran, S. Sriram, W. Withayachumnankul, B. T. Kuhlmey, and S. Atakaramians, "Broadband Single-Mode Hybrid Photonic Crystal Waveguides for Terahertz Integration on a Chip," Adv. Mater. Technol. **5**(7), 2000117 (2020).
18. F. Fesharaki, T. Djerafi, M. Chaker, and K. Wu, "Guided-wave properties of mode-selective transmission line," IEEE Access **6**, 5379–5392 (2018).
19. K. Nielsen, H. K. Rasmussen, A. J. Adam, P. C. Planken, O. Bang, and P. U. Jepsen, "Bendable, low-loss Topas fibers for the terahertz frequency range," Opt. Express **17**(10), 8592–8601 (2009).
20. J. Yang, J. Zhao, C. Gong, H. Tian, L. Sun, P. Chen, L. Lin, and W. Liu, "3D printed low-loss THz waveguide based on Kagome photonic crystal structure," Opt. Express **24**(20), 22454–22460 (2016).
21. B. Hong, M. Swithenbank, N. Greenall, R. G. Clarke, N. Chudpooti, P. Akkaraekthalin, N. Somjit, J. E. Cunningham, and I. D. Robertson, "Low-loss asymptotically single-mode THz Bragg fiber fabricated by digital light processing rapid prototyping," IEEE Trans. Terahertz Sci. Technol. **8**(1), 90–99 (2018).
22. H. Bao, K. Nielsen, O. Bang, and P. U. Jepsen, "Dielectric tube waveguides with absorptive cladding for broadband, low-dispersion and low loss THz guiding," Sci. Rep. **5**(1), 7620 (2015).
23. H. Bao, K. Nielsen, H. K. Rasmussen, P. U. Jepsen, and O. Bang, "Fabrication and characterization of porous-core honeycomb bandgap THz fibers," Opt. Express **20**(28), 29507–29517 (2012).
24. M. Navarro-Cía, J. E. Melzer, J. A. Harrington, and O. Mitrofanov, "Silver-coated Teflon tubes for waveguiding at 1–2 THz," J. Infrared, Millimeter, Terahertz Waves **36**(6), 542–555 (2015).
25. P. Yeh, A. Yariv, and E. Marom, "Theory of Bragg fiber," J. Opt. Soc. Am. B **68**(9), 1196–1201 (1978).
26. P. Lova, G. Manfredi, L. Boarino, A. Comite, M. Laus, M. Patrini, F. Marabelli, C. Soci, and D. Comoretto, "Polymer distributed bragg reflectors for vapor sensing," ACS Photonics **2**(4), 537–543 (2015).
27. H. Qiu, J. Jiang, P. Yu, T. Dai, J. Yang, H. Yu, and X. Jiang, "Silicon band-rejection and band-pass filter based on asymmetric Bragg sidewall gratings in a multimode waveguide," Opt. Lett. **41**(11), 2450–2453 (2016).
28. A. R. Weily, K. P. Esselle, and B. C. Sanders, "Layer-by-layer photonic crystal horn antenna," Phys. Rev. E **70**(3), 037602 (2004).
29. G. Singh, J. D. B. Bradley, N. Li, E. S. Magden, M. Moresco, T. N. Adam, G. Leake, D. Coolbaugh, and M. R. Watts, "Resonant pumped erbium-doped waveguide lasers using distributed Bragg reflector cavities," Opt. Lett. **41**(6), 1189–1192 (2016).
30. A. Abdolvand, A. M. Walser, M. Ziemienczuk, T. Nguyen, and P. S. T. Russell, "Generation of a phase-locked Raman frequency comb in gas-filled hollow-core photonic crystal fiber," Opt. Lett. **37**(21), 4362–4364 (2012).
31. P. Yeh and A. Yariv, "Bragg reflection waveguides," Opt. Commun. **19**(3), 427–430 (1976).
32. J. Dai, J. Zhang, W. Zhang, and D. Grischkowsky, "Terahertz time-domain spectroscopy characterization of the far-infrared absorption and index of refraction of high-resistivity, float-zone silicon," J. Opt. Soc. Am. B **21**(7), 1379–1386 (2004).
33. Y. Xu, R. K. Lee, and A. Yariv, "Asymptotic analysis of Bragg fibers," Opt. Lett. **25**(24), 1756–1758 (2000).
34. Y. Zhang and I. D. Robertson, "Analysis and design of Bragg fibers using a novel confinement loss diagram approach," J. Lightwave Technol. **28**(22), 3197–3206 (2010).
35. J. D. Joannopoulos, S. G. Johnson, J. N. Winn, and R. D. Meade, *Photonic Crystals: Molding the Flow of Light*, 2nd edition, (Princeton University, 2008).
36. S. G. Johnson and J. D. Joannopoulos, "Block-iterative frequency-domain methods for Maxwell's equations in a planewave basis," Opt. Express **8**(3), 173–190 (2001).
37. P. Yeh, A. Yariv, and C.-S. Hong, "Electromagnetic propagation in periodic stratified media. I. General theory," J. Opt. Soc. Am. **67**(4), 423–438 (1977).
38. B. Hong, M. Swithenbank, N. Somjit, J. Cunningham, and I. Robertson, "Asymptotically single-mode small-core terahertz Bragg fibre with low loss and low dispersion," J. Phys. D: Appl. Phys. **50**(4), 045104 (2017).
39. N. A. Issa, A. Argyros, M. A. van Eijkelenborg, and J. Zagari, "Identifying hollow waveguide guidance in air-cored microstructured optical fibres," Opt. Express **11**(9), 996 (2003).
40. IEEE Std 1785.1-2012, "IEEE Standard for Rectangular Metallic Waveguides and Their Interfaces for Frequencies of 110 GHz and Above – Part 1: Frequency Bands and Waveguide Dimensions".
41. F. Xu and K. Wu, "Guided-wave and leakage characteristics of substrate integrated waveguide," IEEE Trans. Microwave Theory Tech. **53**(1), 66–73 (2005).
42. R. B. Marks, "A multiline method of network analyzer calibration," IEEE Trans. Microwave Theory Tech. **39**(7), 1205–1215 (1991).